

JGR Space Physics

RESEARCH ARTICLE

10.1029/2020JA028726

Key Points:

- Measurements of nighttime thermospheric neutral winds made by Ionospheric Connection Explorer-Michelson Interferometer Global High-resolution Thermospheric Imaging agree with ground-based Fabry-Perot interferometer measurements to within 10 m/s
- The comparison validates the independent zero-wind removal and analysis processes employed by these instruments

Correspondence to:

J. J. Makela,
jmakela@illinois.edu

Citation:

Makela, J. J., Baughman, M., Navarro, L. A., Harding, B. J., Englert, C. R., Harlander, J. M., et al. (2021). Validation of ICON-MIGHTI thermospheric wind observations: 1. Nighttime Red-line Ground-Based Fabry-Perot Interferometers. *Journal of Geophysical Research: Space Physics*, 126. <https://doi.org/10.1029/2020JA028726>

Received 22 SEP 2020

Accepted 7 DEC 2020

Validation of ICON-MIGHTI Thermospheric Wind Observations: 1. Nighttime Red-Line Ground-Based Fabry-Perot Interferometers

Jonathan J. Makela¹ , Matthew Baughman¹, Luis A. Navarro¹ , Brian J. Harding² , Christoph. R. Englert³ , John M. Harlander⁴ , Kenneth D. Marr³, Zouhair Benkhaldoun⁵ , Mohamed Kaab⁵, and Thomas J. Immel²

¹Department of Electrical and Computer Engineering, University of Illinois at Urbana-Champaign, Urbana, IL, USA,

²Space Sciences Laboratory, University of California, Berkeley, CA, USA, ³Space Science Division, U.S. Naval Research Laboratory, Washington, DC, USA, ⁴Space Systems Research Corporation, Alexandria, VA, USA, ⁵Laboratory of High Energy Physics and Astrophysics, Oukaimeden Observatory, FSSM, Cadi Ayyad University, Marrakech, Morocco

Abstract Observations of the nighttime thermospheric wind from two ground-based Fabry-Perot Interferometers are compared to the level 2.1 and 2.2 data products from the Michelson Interferometer Global High-resolution Thermospheric Imaging (MIGHTI) onboard National Aeronautics and Space Administration's Ionospheric Connection Explorer to assess and validate the methodology used to generate measurements of neutral thermospheric winds observed by MIGHTI. We find generally good agreement between observations approximately coincident in space and time with mean differences less than 11 m/s in magnitude and standard deviations of about 20–35 m/s. These results indicate that the independent calculations of the zero-wind reference used by the different instruments do not contain strong systematic or physical biases, even though the observations were acquired during solar minimum conditions when the measured airglow intensity is weak. We argue that the slight differences in the estimated wind quantities between the two instrument types can be attributed to gradients in the airglow and thermospheric wind fields and the differing viewing geometries used by the instruments.

Plain Language Summary This study presents a validation of observations made by two different types of instruments used to measure nighttime thermospheric neutral winds. These winds represent the motion of neutral particles in the thermosphere and studying their properties is critical to gaining a complete understanding of the dynamics of the Earth's upper atmosphere. We use observations made by two ground-based Fabry-Perot interferometers to validate measurements from the Michelson Interferometer for Global High-resolution Thermospheric Imaging (MIGHTI) onboard National Aeronautics and Space Administration's recently launched Ionospheric Connection Explorer satellite. After identifying observations from the different instruments that are coincident in space and time, we show that the measurements are statistically highly correlated, thereby successfully validating the MIGHTI thermospheric wind observations.

1. Introduction

Thermospheric neutral winds play a key role in determining the state and evolution of Earth's upper atmosphere. Their interplay with the ionosphere through plasma transport and generation of polarization electric fields set up the diurnal electrodynamics in this region. They push the plasma along the Earth's magnetic field lines, strongly affecting the altitude distribution of plasma density (particularly at midlatitudes) and also the amount of ionization by moving the plasma to regions with different recombination rates (Rishbeth, 1972; Rishbeth & Garriot, 1969). Thus, their accurate global monitoring and specification is important for a better understanding of the state of our near-space environment.

Several studies have led to a good understanding of the climatological features of the solar-quiet upper thermospheric wind circulation. Winds are mainly driven by horizontal pressure gradients imposed by the diurnal bulge, generated by the absorption of extreme ultraviolet radiation and regulated by the ion-drag force exerted mostly by neutral-ion collisions (Kelley, 2009; Rishbeth & Garriot, 1969). This circulation can

be severely affected by geomagnetic activity as well as by forcing coming from lower altitude regions of the atmosphere.

During periods of strong geomagnetic activity, the wind circulation can be affected by global and long-lasting disturbance winds generated primarily by the action of Joule heating at high latitudes (e.g., Richmond, 1979; Richmond & Matsushita, 1975). More recently, Xiong et al. (2015) investigated the global features of the thermospheric disturbance winds and found that they are westward and strongest at nighttime with stronger magnitudes for higher latitudes. At midlatitudes, these disturbances can reach westward magnitudes of about 150 m/s early in the night, and reach largest equatorward magnitudes in the post-midnight sector (Fejer et al., 2002). Moreover, Navarro and Fejer (2019, 2020) found large nighttime wind disturbances around midnight that lasted for about two nights in the equatorial region.

Similarly, other sources like gravity waves coming from lower regions of the atmosphere with large temporal and horizontal scales can impose significant spatial and temporal variability in the thermosphere. The gravity wave activity interacts with the background wind at lower altitudes and plays an important role in the dissipation, momentum deposition, and net heating/cooling in the thermosphere (e.g., Lu et al., 2009; Richmond, 1978; Vadas, 2007; Vadas & Fritts, 2004). Forbes et al. (2016) used mass densities and winds at thermospheric altitudes derived from accelerometer measurements on the Gravity Field and Ocean Circulation Earth Explorer satellite to study the global morphology of horizontal structures between 128 and 640 km, which are assumed to mainly reflect the presence of gravity waves.

Despite the comprehensive understanding of the effects of these sources on the thermosphere, there are fundamental questions regarding the role of the different competing sources over the thermospheric winds, in particular for the ones coming from below during low solar flux activity periods (Immel et al., 2017; Xiong et al., 2019) and for thermospheric weather (Harding et al., 2019).

Thermospheric winds have been generally measured remotely by passive optical instrumentation. These instruments measure the Doppler shift and broadening of the spectra of various faint and naturally occurring emission lines known as airglow, resulting from different chemical reactions occurring in the thermosphere. One of the most used instrument types to make these measurements are optical spectrometers and, in particular, the Fabry-Perot interferometer (FPI; e.g., Biondi et al., 1999; Brum et al., 2012; Hernandez & Roble, 1979; Kaab et al., 2017; Meriwether, 2006; Meriwether et al., 2013; Shiokawa et al., 2003). FPIs have proved to be efficient for such observations and have become somewhat portable and easier to operate in recent years (Makela et al., 2013, 2009), allowing for the development of several ground-based networks used to make wider-scale measurements (Makela et al., 2012; Meriwether, 2006). However, there are currently not enough FPIs deployed to provide global coverage of the thermospheric winds. Furthermore, since these FPIs are ground-based instruments, they are generally confined to measure during the nighttime period only, observe the integrated signal along specific line-of-sights (LOSs), and can be strongly affected by atmospheric scattering (Harding, Makela, Qin et al., 2017).

On the other hand, optical instrumentation on satellites are able to overcome these limitations and to provide altitudinal, longitudinal, and latitudinal measurements of the thermospheric winds. This was the case, for example, for the Wind Imaging Interferometer (WINDII) onboard the Upper Atmosphere Research Satellite (UARS) which employed a limb-scanning Michelson interferometer (Shepherd et al., 1993). The observations from this instrument were validated against and compared to different Michelson, Fabry-Perot interferometers, and radars (Duboin, 1997; Gault et al., 1996; Lathuillère et al., 1997). The comparisons were generally good, in some cases agreeing to within 10 m/s, with some of the differences attributed to gravity wave activity at different seasons and to differences in the observing geometries of the instruments (Shepherd et al., 2012). Concerted effort was made to resolve these disagreements and the data served to improve the most widely used empirical wind model (Drob et al., 2008; Emmert et al., 2008).

More recently, the Michelson Interferometer for Global High-resolution Thermospheric Imaging (MIGHTI) onboard National Aeronautics and Space Administration's (NASA's) Ionospheric Connection Explorer (ICON; Immel et al., 2017) used the Doppler Asymmetric Spatial Heterodyne (DASH) technique to measure thermospheric neutral winds. This technique is an improvement over the Michelson interferometer used in WINDII which needed moving interferometric parts. MIGHTI is able to take interferogram samples measured simultaneously for different emission lines (Englert et al., 2015, 2017) across a range of altitudes.

The DASH technique was previously compared to the FPI measurement technique by Englert et al. (2012), who compared collocated ground-based neutral wind measurements derived from the Redline DASH Demonstration Instrument to those from an FPI at Pisgah Astronomical Research Institute, South Carolina (35°N, 83°W). They found generally good agreement between both techniques.

This paper presents the first comparison of the ICON-MIGHTI neutral wind measurements with ground-based FPIs at midlatitudes. It serves as a cross-validation of the two measurement techniques and demonstrates that the MIGHTI wind measurements can be employed to study the global distribution of thermospheric neutral winds. Section 2 describes the instrumentation and data processing used for this comparison and describes each of the observing geometries as well as the methodology used to compare the coincident data. Section 3 presents the results of the direct comparisons between measurements of nighttime thermospheric neutral winds made by the two instruments. Finally, Sections 4 summarizes the main results presented on this work.

2. Instrumentation and Methodology

In this study, we use nighttime thermospheric neutral winds derived from observations by two ground-based FPIs and from the MIGHTI (Englert et al., 2017) on the NASA's ICON (Immel et al., 2017) satellite to assess the accuracy of the estimates from these two different observing techniques and platforms.

These instruments observe the Doppler shifted spectra of the 630-nm oxygen emission line to estimate the bulk motion of the thermalized oxygen atoms in the thermosphere along specific LOS directions. The source of these emissions is attributed to the forbidden transitions from the metastable states 1D of excited oxygen atoms, and the mechanism of the excitation of these atoms is related to the dissociative recombination of the O_2^+ to yield O^+ and $O({}^1D)$ (Bates, 1982; Link & Cogger, 1988).

These two instrument types use different interferometric principles and observing geometries giving rise to specific assumptions in the analysis of their observations. Thus, a cross comparison of the resultant neutral wind estimates is useful in examining the robustness of each measurement technique.

In this section, we briefly describe the two measurement techniques as well as the procedure that builds the data set of the MIGHTI and FPI measurements used for this comparative analysis. The estimates from both instruments are compared in both the MIGHTI LOS frame of reference and the cardinal direction frame of reference. In order to properly compare these data sets, we define coincidence metrics to only use FPI and MIGHTI measurements that correspond to approximately the same location at the same time.

2.1. MIGHTI Instrumentation

The MIGHTI instrument employs two separate Michelson interferometers, referred to as MIGHTI-A and MIGHTI-B, to observe the airglow along two orthogonal fields of view, or LOS pointing directions, nominally pointing 45° and 135° in azimuth from the spacecraft velocity vector. Each interferometer acquires a two-dimensional image in which each pixel relates to a coordinate in tangent altitude versus optical path distance space which can be related to the altitudinal distribution of wind velocity (Harding, Makela, Englert et al., 2017). Each MIGHTI interferometer makes observations of both the red- and green-line oxygen emissions during both day and night. In this study, we limit ourselves to studying the results from the red-line emission at night. Several artifact corrections, like using two on-board calibration lamps to monitor thermal drifts in the interferometric phase shifts, are applied to these images as part of the generation of MIGHTI level 1 data products. The retrieval of LOS winds is dependent on the Doppler reference corresponding to the rest wavelength of the emission, that is the wavelength of the emission under zero Doppler shift, generally referred as zero-wind phase reference.

These LOS estimates are representative of the thermospheric winds at the tangent altitude and are referred to as MIGHTI level 2.1 data product. The geometry of the interferometers onboard ICON allows MIGHTI to look along at the same volume every ~8 min along the satellite track from orthogonal directions. This allows for the determination of the horizontal wind vector in the zonal (eastward) and meridional (northward) frame of reference. These data, derived from both MIGHTI-A and MIGHTI-B level 2.1 data products are referred to as the MIGHTI level 2.2 data product.

For this study, we used version 3.0 of the MIGHTI levels 2.1 and 2.2 data products of the nighttime red-line thermospheric winds. They have an altitude sampling of 10 km and a temporal sampling cadence of 60 s. For this data product's version, the zero wind phase has been determined by comparing a 60 days average of MIGHTI data to a 60 days average of the empirical Horizontal Wind Model 2014 (HWM14; Drob et al., 2015), which is a fit to decades of previous wind measurements. To determine the zero-wind reference, at each time and location of a MIGHTI measurement, the MIGHTI measurement is simulated by integrating HWM14 along the line of sight, weighted by the observed volume emission rate (VER) as determined by the measured fringe amplitude profile. The 60 days average difference between the measured and simulated phases is taken as the zero wind phase. This is done separately for each sensor (A and B), for each color (red and green), for each mode (day and night), and for each row (i.e., each altitude). This approach to determining the zero wind phase is analogous to the approach taken for the UARS/HRDI instrument (Hays & HRDI Science Team, 1992), which assumed that a long-term average of the meridional wind is zero. Although the long-term average altitude profile is constrained to match HWM14 in this initial MIGHTI data release, measured variations in time, latitude, longitude, and from day-to-day are retained using this approach.

Future data releases will leverage ICON's unique zero wind maneuver to determine an independent zero wind phase. These maneuvers consist of observing along the same volume from opposite directions, along the ram and wake side of the spacecraft velocity, within a short period of time. The interferometric images along these projections are used to get an estimation of the zero-wind phase as both observations should add up to zero. This maneuver is performed once a month (Harding, Makela, Englert et al., 2017).

2.2. FPI Instrumentation

The ground-based wind measurements used in this study were derived from the FPIs located at the Oukaimeden Observatory near Marrakesh, Morocco (MOR; geographic coordinates: 31.21°N, 7.87°W) and at Urbana, Illinois (UAO; geographic coordinates: 40.17°N, 88.16°W). These instruments observe the airglow along specific LOS by using a dual-axis mirror system to cycle observations through the four cardinal directions (at an elevation angle of 45°), the zenith look direction, and a calibration measurement of a frequency-stabilized He-Ne laser. More details on the instrumentation can be found in Makela et al. (2009).

Observations of the frequency-stabilized laser are used to monitor the thermal drifts and optical aberrations present in the observed spectra caused by the optical system. The instrument parameters estimated by observing the laser are later used to analyze the images taken of the sky. The laser and zenith images are also combined to estimate a reference Doppler velocity to finally calculate an estimate of the LOS thermospheric winds. In short, observations of the frequency-stabilized laser are used to monitor the effects of any temporal changes in the FPI on the observed Doppler shift. This is then translated to the observations of the sky by assuming that the average vertical wind observed looking toward zenith over the course of the night is zero. This process establishes a zero-reference Doppler velocity from which absolute estimates of the horizontal winds can be obtained. More details on this procedure are found in Makela et al. (2011) and Harding et al. (2014). From the LOS estimates, a full horizontal wind vector in the zonal (eastward) and meridional (northward) frame of reference is calculated following Makela et al. (2012).

Other considerations like less favorable viewing conditions caused by cloud cover were taken into account in the data processing. These conditions were monitored using sky temperature measurements from a Boltwood Cloudsensor II system. Moreover, estimates with abnormally large magnitudes (≥ 200 m/s) or large uncertainties (≥ 50 m/s) were removed from consideration. The measurements were made using an observing elevation angle of 45° and thus are representative of the wind 250 km away from the instrument geographic location (assuming an emission altitude of 250 km) in the corresponding cardinal direction.

2.3. Data Coincidence

For the FPI and MIGHTI data sets to be compared, the measurements derived by both instruments must correspond to approximately coincident locations at about the same time. Figure 1 shows the instruments' viewing geometries under which these conditions are achieved. In this figure, the m th MIGHTI LOS is shown as a dashed line and the tangential point of this line and the corresponding n th atmospheric emission

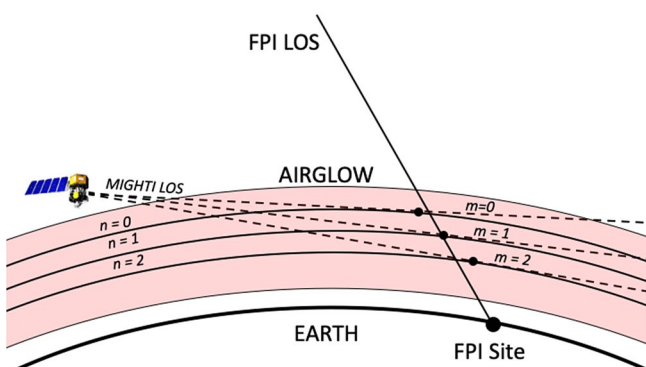


Figure 1. Viewing geometry of MIGHTI and FPI observations. FPI, Fabry-Perot interferometer; MIGHTI, Michelson Interferometer for Global High-resolution Thermospheric Imaging.

many different symmetric layers of Earth's atmosphere as part of the generation of the MIGHTI level 2.1 data product. However, due to the differing viewing geometries, comparisons from the two instruments should not exactly match even when they are pointed to about the same common volume due to the differing gradients in the VER and wind fields.

In order to best compare the altitude-resolved MIGHTI observations to the altitude-integrated FPI ones, the MIGHTI altitude profile must be integrated in altitude taking into account the VER at each altitude. This is accomplished using the normalized VER, $E(z)$ as weights. It is calculated from the VER, $e(z)$, at each altitude, z , and the total VER in altitude:

$$E(z) = \frac{e(z)}{\int_z e(z) dz} \quad (1)$$

Thus, the height-integrated MIGHTI wind estimate, V_{int} , is calculated by,

$$V_{int} = \int_z V(z)E(z)dz \quad (2)$$

Then, V_{int} is ascribed at the tangent location of the peak altitude of the MIGHTI VER profile. This procedure avoids the common assumption that FPI winds can be attributed to a specific altitude (e.g., 250 km) and ensures a more accurate comparison between ground-based and space-based winds.

This calculation is made for both MIGHTI levels 2.1 and 2.2 data products for comparisons to FPI-derived horizontal winds. For the level 2.2 data products, the MIGHTI and FPI winds are in the same reference frame (zonal/meridional winds). However, for the level 2.1 comparisons we need to calculate the projection of the FPI wind vector estimate along the MIGHTI LOS direction. This is performed using the following operation:

$$V_{LOS} = U_{FPI} \sin(\theta) + V_{FPI} \cos(\theta) \quad (3)$$

where V_{LOS} is the FPI wind estimate along the MIGHTI-A/B look direction, U_{FPI} and V_{FPI} are the zonal and meridional winds measured by the FPI, respectively, and θ is the azimuth angle of the LOS of the MIGHTI-A/B look direction, at the tangent location, measured in degrees east of north. Note that V_{LOS} is calculated from U_{FPI} and V_{FPI} which are acquired sequentially looking in different directions from the FPI, and are thus separated by ~ 350 km in space. Thus, in the calculation of V_{LOS} there is an inherent assumption about the uniformity of the wind field in space and time over ~ 350 km and several minutes.

In this study, the criteria employed to determine data coincidence is a MIGHTI measurement within 500 km spatially and 30 min temporally of an FPI measurement. For comparisons of level 2.1 data products (LOS), we define the FPI measurement to be at the location of the FPI instrument, due to the spatially averaged

layer are shown as black dots. As indicated before, MIGHTI level 2.1 data product, or LOS wind estimates, are representative of the projection of the thermospheric winds along this LOS at the tangential point. Similarly, the FPI LOS is shown as a solid line from the FPI location on the ground. Its corresponding LOS observation is representative of the thermospheric wind along this LOS at the peak emission height.

Figure 1 shows that the LOS wind measurements from both instruments are integrated observations along long paths through the atmosphere. These measurements are, essentially, VER weighted averages of the winds along the corresponding LOS. The VER profile used here is obtained from the MIGHTI products. It is the inverted fringe amplitude, modified by a factor to account for the fringe visibility reduction due to atmospheric temperature. Atmospheric temperature is obtained from MSIS. Although the MIGHTI VER product is not absolutely calibrated, absolute calibration is not required for the analysis used here. Note that some of the effects of VER variations along the LOS are considered in the Abel-like inversion process that takes into account contributions from

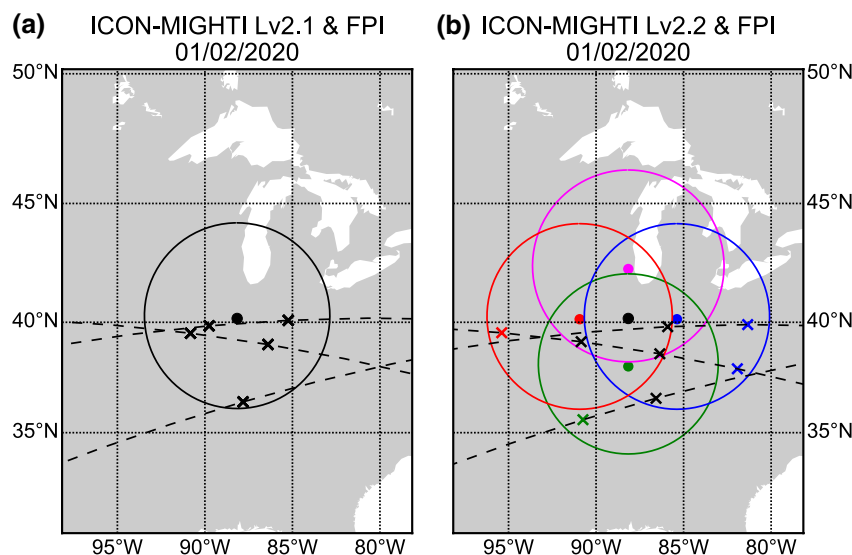


Figure 2. Example coincident measurements between FPI observations and (a) MIGHTI level 2.1 data products and (b) MIGHTI level 2.2 data product made over Urbana, Illinois on January 2, 2020. The dashed lines represent MIGHTI observational paths on consecutive ICON orbits. The “x” markers represent MIGHTI observations that are deemed coincident with FPI observations. Small solid circles represent the 250-km altitude pierce point of the FPI observations in the cardinal directions while the larger circles represent the 500-km radius in which a MIGHTI observation must fall to be considered coincident with an FPI measurement. In (b), the circles are color-coded based on the individual cardinal look directions. Similarly, the “x” markers are coded by color, with black “x”s denoting when a level 2.2 observation is coincident with multiple FPI look directions. FPI, Fabry-Perot interferometer; ICON, Ionospheric Connection Explorer; MIGHTI, Michelson Interferometer for Global High-resolution Thermospheric Imaging.

FPI horizontal winds required to compute V_{LOS} . For comparisons to level 2.2, the FPI measurement location is defined as the 250-km pierce point of a given cardinal look direction. Only coincidences that have a MIGHTI quality flag of 1, indicating “good” data quality, and FPI data that passes the quality constraints described in Section 2.2 are considered. For multiple coincident data points within our criteria for a single satellite pass, we choose the closest in time.

Figures 2a and 2b show examples of coincidences for level 2.1 and 2.2 data products, respectively, that matches our spatial and temporal coincidence criteria. These examples are for the UAO FPI location and show the corresponding observational paths (dashed lines) and tangential locations (“x” marks) of MIGHTI wind estimates on consecutive ICON orbits on January 1, 2020.

Figure 2a shows the coincidence MIGHTI geographic locations for the level 2.1 product comparison and uses the FPI geographic location to define the 500-km circular region to define our spatial coincidence threshold. Figure 2b shows the corresponding MIGHTI locations for the level 2.2 comparison and, therefore, uses several circular regions to define our spatial coincidence threshold for each FPI look direction. Note, that in the level 2.2 comparisons, each MIGHTI observation point has both components of the horizontal vector wind. As a result, MIGHTI measurement's the lie within the intersection of, for example, the south and west FPI look directions can be independently compared to FPI meridional and zonal wind measurements.

To illustrate the comparison methodology using the VER-weighted, height-integrated MIGHTI winds to the FPI winds, Figure 3 shows the data coincidence comparisons for each level of MIGHTI data products using MOR FPI winds and two altitude profiles of MIGHTI winds. Each figure shows the MIGHTI altitude profile (blue line), the VER-weighted, height-integrated MIGHTI winds (orange vertical line, calculated using Equation 2), and the coincident FPI wind estimates. The orange and blue shadings of the height-integrated and of the altitude profile of MIGHTI winds correspond to standard deviations of the observations. Note that the FPI wind estimates are placed at the observed peak altitude of the VER altitude profile which is also shown on each figure and marked with a horizontal line. The red portion of the VER altitude profile indicates altitudes where the MIGHTI analysis has indicated that the data quality is “good” while the black

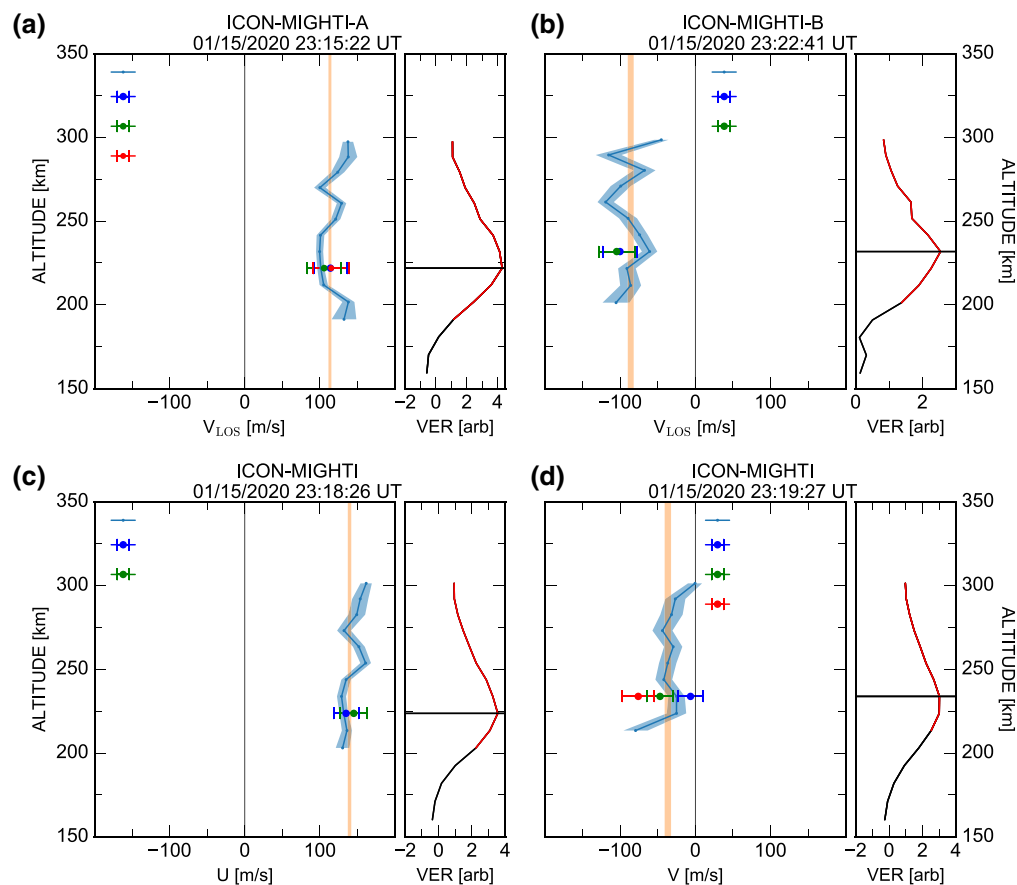


Figure 3. Example vertical altitude profiles of (a) level 2.1 MIGHTI-A, (b) level 2.1 MIGHTI-B, (c) level 2.2 zonal wind, and (d) level 2.2 meridional wind comparisons to FPI measurements made from the Morocco observation site on January 15, 2020. Coincident FPI measurements are displayed as points located at the altitude of peak VER with the difference in time between MIGHTI and FPI measurements given in the legend. For (a) and (b), the closest FPI measurements are rotated onto the MIGHTI-A/B line of sight using Equation 3. Only the measurements closest in time are utilized in the statistical analysis presented here. FPI, Fabry-Perot interferometer; MIGHTI, Michelson Interferometer for Global High-resolution Thermospheric Imaging; VER, volume emission rate.

portion represents the portion of VER profile with “caution” or “bad” data quality. Only “good” quality observations are used in our analysis. Each of the FPI wind estimates also shows the temporal criteria, that is, the time difference in seconds between the MIGHTI and FPI observations.

3. Results

Using the methodology described above, we have compared thermospheric neutral wind measurements made by ground-based FPIs located at the Oukaimeden Observatory near Marrakesh, Morocco (MOR; geographic coordinates: 31.206°N, 7.866°W) and Urbana, Illinois (UAO; geographic coordinates: 40.167°N, 88.159°W) and MIGHTI level 2.1 and 2.2 data products. All coincident measurements, as defined in Section 2.3, over the period of January 1, 2020 through May 31, 2020 have been considered. Due to the orbit design of the ICON satellite and local observing conditions at the observatories, we do not get a usable coincidence for a given FPI site on every night.

In the sections below, we present the results of the comparison between the thermospheric neutral winds made by the FPIs and MIGHTI. These results are separately presented for comparisons to the MIGHTI level 2.1 and 2.2 data products. Due to the implementation of the VER-weighted wind calculation for MIGHTI measurements, the existence of altitude gradients in horizontal wind velocities, and a difference in space and time between MIGHTI and FPI observations, the comparisons between the FPI and MIGHTI data sets

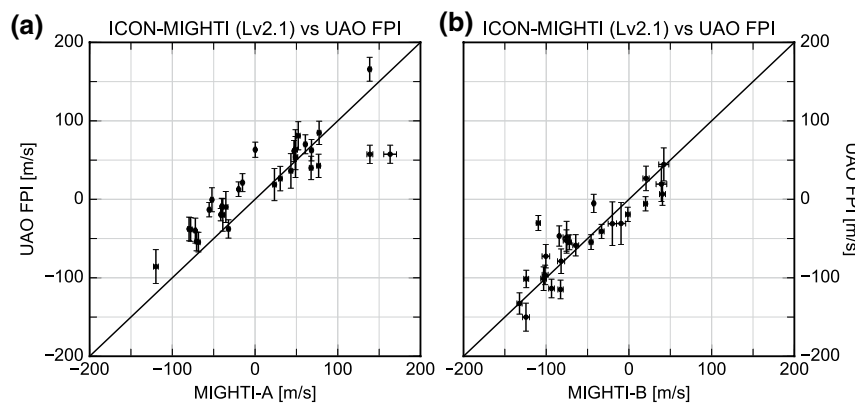


Figure 4. Comparison between thermospheric wind measurements made by the FPI at Urbana and MIGHTI along the (a) MIGHTI-A line-of-sight and (b) MIGHTI-B line-of-sight. The diagonal line represents a perfect match between the two data sets. FPI, Fabry-Perot interferometer; MIGHTI, Michelson Interferometer for Global High-resolution Thermospheric Imaging.

are not expected to yield an exact 1:1 match. We take a statistical approach to analyze the two data sets, characterizing the comparison by the average and the standard deviation of the difference between the FPI and MIGHTI wind measurements, as well as their Pearson correlation coefficient. If the average difference between data sets is within one standard deviation of the ideal difference of 0 then the data sets can be determined to be statistically similar. The level 2.1 and level 2.2 data comparisons are given in Sections 3.1 and 3.2, respectively.

3.1. Level 2.1 Data Comparison

All level 2.1 MIGHTI-A and MIGHTI-B coincidences with the UAO FPI measurements that satisfy the criteria are utilized, processed as described above, and presented in Figure 4. 31 (26) comparisons with MIGHTI-A (MIGHTI-B) are presented. Uncertainties for both measurements are shown using error bars, although we note that because the MIGHTI measurements are made averaging together multiple measurements with relatively small individual uncertainties, the statistical uncertainties of the weighted average are typically too small to be seen in this display. In addition, the MIGHTI uncertainties account for statistical error only, and do not include systematic errors from calibrations or zero-wind errors. The diagonal line indicates the line of perfect agreement. Deviations from this line indicate differences in the measured thermospheric winds from the two instruments measured at nearly the same time and location. As mentioned above, we do not expect perfect agreement. However, the fact that over the 5 months of data presented here the general trend follows this line is very encouraging and indicates that MIGHTI is operating as expected.

We take a more detailed look at the comparisons by computing statistics for all coincidences. Table 1 shows the mean difference between the FPI and MIGHTI measurements (calculated as FPI – MIGHTI) as well as the standard deviation of this difference for the comparison to UAO. The mean differences calculated for

each MIGHTI instrument (MIGHTI-A: 10.71 m/s; MIGHTI-B: 2.77 m/s) are indicative of larger magnitudes measured by the FPIs within a reasonable range given the design requirements of the MIGHTI instrument for nighttime thermospheric measurements. Note that the average uncertainties of the FPI and MIGHTI nighttime observations used in this study are ~ 15 and ~ 5 m/s, respectively. Thus, the mean differences reported here are smaller than the combined uncertainties of these two measurements ($\sqrt{15^2 + 5^2} = 15.8$ m/s). The Pearson correlation coefficient is also shown in the table, and indicates strong correlation between the two data sets.

Table 1

Statistics of the Comparisons of Nighttime Thermospheric Wind Measured by the Ground-Based FPI at Urbana, Illinois Site and the Satellite-Based MIGHTI Broken up by MIGHTI Line-of-Sight

	N	$\mu_{\text{FPI-MIGHTI}}$	$\sigma_{\text{FPI-MIGHTI}}$	Pearson correlation coefficient
MIGHTI-A	31	10.71 m/s	35.49 m/s	0.88
MIGHTI-B	26	2.77 m/s	26.23 m/s	0.88

FPI, Fabry-Perot interferometer; MIGHTI, Michelson Interferometer for Global High-resolution Thermospheric Imaging.

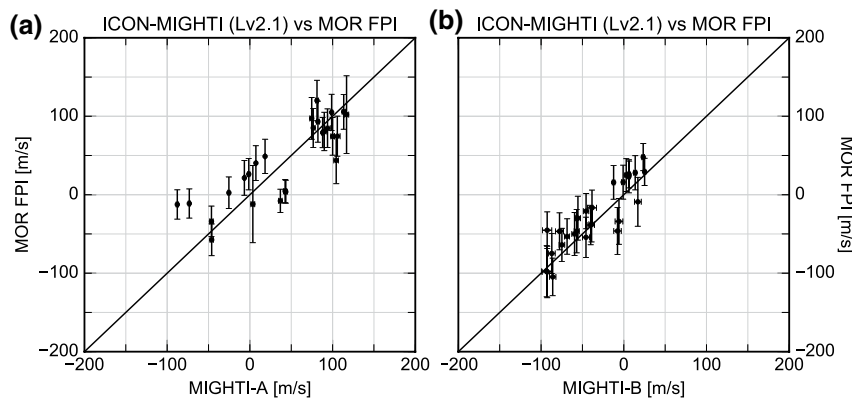


Figure 5. Same as Figure 4, but for the FPI at Morocco. FPI, Fabry-Perot interferometer.

Figure 5 and Table 2 present similar information for comparisons between MIGHTI and MOR. For this site, 26 (27) comparisons are available for MIGHTI-A (MIGHTI-B) over the time frame of this study. The mean difference between the FPI and MIGHTI measurements are small (MIGHTI-A: 2.62 m/s; MIGHTI-B: 8.42 m/s) and the correlation between the two data sets is strong. This is in general agreement with the comparisons seen above between MIGHTI and UAO.

3.2. Level 2.2 Data Comparison

We also compare the thermospheric winds provided in the cardinal coordinate frame (zonal and meridional components) from the level 2.2 MIGHTI data product and the ground-based FPIs. Figure 6 shows the comparison of the entire data set recorded at the two FPI observation locations and MIGHTI observation data. Only data points that are deemed coincident based on the criteria given in Section 2.3 are compared. Again, the diagonal line indicates perfect agreement between the two measurements and the error bars represent the uncertainty of the measurements.

Table 3 gives the statistics of the difference between the FPI and MIGHTI measurements displayed in Figure 6. 56 (71) coincidences are found with UAO (MOR). Similar to what was seen for comparison to the level 2.1 data product, the mean difference between the FPI and MIGHTI observations is small: 7.29 m/s for UAO and 3.64 m/s for MOR. The standard deviations of the differences are also quite reasonable, 26.18 m/s for UAO and 34.48 m/s for MOR. Strong correlation is also seen between MIGHTI measurements and the ground-based instruments. The (blue) zonal and (red) meridional components of the winds are shown in Figure 6, however, no significant differences in the statistics were found when considering the individual components (not shown).

4. Discussion and Conclusions

The analysis presented in this paper was performed to validate the current methodology used to generate measurements of nighttime thermospheric winds observed by the MIGHTI, with a primary focus on

the zero-wind reference used by MIGHTI. However, zero-wind determination is necessary for the ground-based FPIs, as well. The methodology for determining this zero wind for the UAO and MOR instruments is described in Makela et al. (2011). This technique could result in an imperfect removal of the unknown zero wind. However, given that the results presented in this paper show very good agreement between the ground-based FPIs and MIGHTI, we are confident that the independent zero-wind removal processes used for MIGHTI-A, MIGHTI-B, UAO, and MOR are valid to within several m/s. If an incorrect zero wind were removed, we would expect the mean differences between the MIGHTI and FPIs to show significant bias, which they do not.

Table 2

Same as Table 1, but for the FPI at Morocco

	n	$\mu_{\text{FPI-MIGHTI}}$	$\sigma_{\text{FPI-MIGHTI}}$	Pearson correlation coefficient
MIGHTI-A	26	2.62 m/s	33.06 m/s	0.85
MIGHTI-B	27	8.42 m/s	19.83 m/s	0.89

FPI, Fabry-Perot interferometer; MIGHTI, Michelson Interferometer for Global High-resolution Thermospheric Imaging.

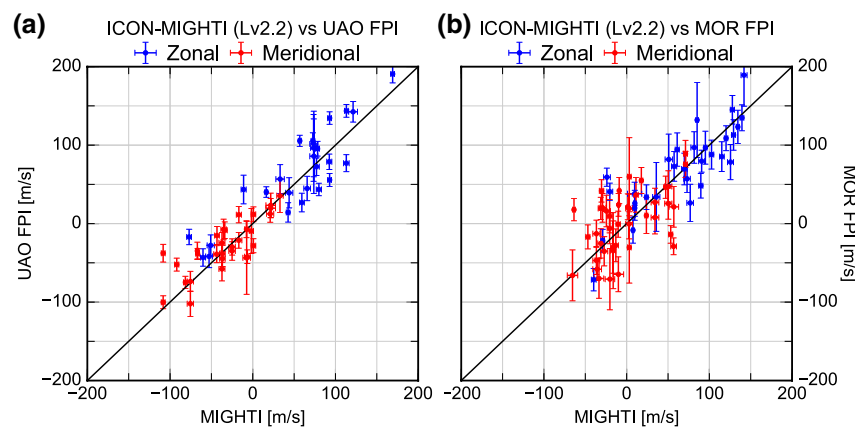


Figure 6. Relationship between wind measured by ground-based FPI at field locations at (a) Urbana, IL and (b) Morocco and wind measured by MIGHTI. Individual measurements are color-coded by (blue) zonal and (red) meridional directions. FPI, Fabry-Perot interferometer; MIGHTI, Michelson Interferometer for Global High-resolution Thermospheric Imaging.

As mentioned above, in all of the comparisons presented here, we see the data sets show strong correlation ($r > 0.80$) with small mean differences ($\mu < 10$ m/s). We assert that this gives confidence in both measurements and acts as a validation of the MIGHTI red-line thermospheric wind measurements during nighttime. Still, the variance in these differences ($\sigma > 20$ m/s) is larger than the combined uncertainties from the individual measurements. This suggests that there is a source of variance above what can be attributed solely to the instruments. The most likely sources of these discrepancies are the differing viewing geometries and geophysical variability.

Gradients in VER and wind along the lines of sight can lead to errors in the estimated wind, as shown through the modeling of Harding, Makela, Englert et al. (2017) for the MIGHTI geometry. This has been further investigated by Wu et al. (2020), who found that errors on the order of 10 m/s can be attributed to this sort of consideration within 30° of the terminator. Although we have removed coincidences involving MIGHTI measurements made near the terminator for this study, the work of Harding, Makela, Englert et al. (2017) and Wu et al. (2020) provide evidence that observing geometry considerations must also be taken into account when cross-validating these types of measurements.

Gault et al. (1996) presented a similar comparison between ground-based FPI measurements made from the Peach Mountain Observatory, Michigan, USA (geographic coordinates: 42.4°N , 83.9°W) and a station at Mount John, New Zealand (geographic coordinates: 44.0°S , 170.5°E) with the WINDII which flew on NASA's UARS from 1991 until 1997. This was a solar maximum period, whereas the MIGHTI measurements to date have been made during a deep solar minimum. The two sites used in the Gault et al. (1996) study are equivalent in latitude to the UAO site used in the current study. Their comparison was made using green-line observations, which originates from an altitude around 97 km at night, in contrast to the MIGHTI red-line observations used here, which originates from an altitude around 250 km at night. Although the altitude range for the comparisons is different, similar viewing geometries are used in both studies and it is instructive to compare results to understand potential geometry-based effects in our analysis.

The Gault et al. (1996) analysis was most similar to our comparison to the MIGHTI level 2.1 data, with the ground-based observations rotated into the observing frame of the satellite measurements and the satellite measurements presented as integrated quantities weighted by the VER. A slightly more relaxed spatial coincidence was utilized (a 1,000-km distance threshold compared to the 500-km threshold used here).

Results of the WINDII-FPI comparison are summarized in Table 5 of Gault et al. (1996). In short, they found mean differences between the

Table 3

Statistics of the Comparisons of Nighttime Thermospheric Wind Measured by Ground-Based FPIs and Satellite-Based MIGHTI Level 2.2 Data

	n	$\mu_{\text{FPI-MIGHTI}}$	$\sigma_{\text{FPI-MIGHTI}}$	Pearson correlation coefficient
UAO	56	7.29 m/s	26.18 m/s	0.92
MOR	71	3.64 m/s	34.48 m/s	0.81

FPI, Fabry-Perot interferometer; MIGHTI, Michelson Interferometer for Global High-resolution Thermospheric Imaging.

instruments that were less than 10 m/s in magnitude and had standard deviations between 20 and 30 m/s. These are quite consistent with what we find for the MIGHTI-FPI comparisons presented here in Tables 1 and 2. The comparable nature of the standard deviations indicate that the combination of differing viewing geometries and natural variation of quantities along viewing directions limits these sorts of cross-validations. Nevertheless, they also provide information about instrumental uncertainties that can inform future studies that include ground- and spaced-based data sets.

It is interesting to note, however, that in the case of the WINDII-FPI comparisons, Gault et al. (1996) found a consistent offset between the two satellite fields-of-view (their ΔFOV1 and ΔFOV2 ; similar in nature to our MIGHTI-A and MIGHTI-B), which might suggest an offset between the different fields-of-view. In the case of MIGHTI, we do not find this to be the case. In the comparison to UAO, the offset between MIGHTI-A and MIGHTI-B is $10.71 - 2.77 = 7.94$ m/s whereas using the MOR comparisons, the offset is $2.62 - 8.42 = -5.80$ m/s. Thus, we conclude that there is no consistent offset between the two MIGHTI instruments and that these differences are more likely attributable to the different viewing geometries over the two sites and gradients in the airglow and thermospheric wind fields due to the differing geophysical characteristics in these regions (i.e., MOR is a low-latitude site closer to the equatorial anomalies whereas UAO is a midlatitude site). As additional data are collected by MIGHTI over varying seasonal and solar cycle conditions, we will be able to more fully investigate these effects.

As additional measurements are collected by MIGHTI over the duration of the ICON mission, additional opportunities for a more detailed and comprehensive study of the thermospheric winds and their connection to lower-atmospheric variability will be conducted. What we have shown here is that the MIGHTI measurements and those made by two ground-based FPIs are consistent with one another, and so MIGHTI nighttime thermospheric wind measurements can be used with confidence. Additional work is currently underway to compare the lower-thermospheric wind observations made by meteor radars made using the green-line emission also measured by MIGHTI.

Data Availability Statement

The MIGHTI data products are available at the website of the ICON mission (<https://icon.ssl.berkeley.edu/>). The FPI data are available through the CEDAR Madrigal database (<http://cedar.openmadrigal.org/openmadrigal/>).

Acknowledgments

ICON is supported by NASA's Explorer Program through contracts NNG-12FA45C and NNG12FA42I. Operation of the FPIs is supported at the University of Illinois at Urbana-Champaign by National Science Foundation CEDAR (Grant nos. AGS 16-51298 and AGS 19-32953).

References

Bates, D. R. (1982). Airglow and Auroras. In H. S. W. Massey, & D. R., Bates (Eds.), *Applied atomic collision physics* (pp. 149–224) New York, NY: Academic Press. <https://doi.org/10.1016/B978-0-12-478801-5.50012-8>

Biondi, M. A., Sazykin, S. Y., Fejer, B. G., Meriwether, J. W., & Fesen, C. G. (1999). Equatorial and low latitude thermospheric winds: Measured quiet time variations with season and solar flux from 1980 to 1990. *Journal of Geophysical Research*, 104(A8), 17091–17106. <https://doi.org/10.1029/1999JA900174>

Brum, C. G. M., Tepley, C. A., Fentzke, J. T., Robles, E., dos Santos, P. T., & Gonzalez, S. A. (2012). Long-term changes in the thermospheric neutral winds over arecibo: Climatology based on over three decades of Fabry-Perot observations. *Journal of Geophysical Research*, 117, A00H14. <https://doi.org/10.1029/2011JA016458>

Drob, D. P., Emmert, J. T., Crowley, G., Picone, J. M., Shepherd, G. G., Skinner, W., & Vincent, R. A. (2008). An empirical model of the Earth's horizontal wind fields: HWM07. *Journal of Geophysical Research*, 113, A12304. <https://doi.org/10.1029/2008JA013668>

Drob, D. P., Emmert, J. T., Meriwether, J. W., Makela, J. J., Doornbos, E., Conde, M., & Klenzing, J. H. (2015). An update to the Horizontal Wind Model (HWM): The quiet time thermosphere. *Earth and Space Science*, 2(7), 301–319. <https://doi.org/10.1002/2014EA000089>

Duboin, M.-L. (1997). Dynamics of the thermosphere: diurnal variations observed by WINDII on board UARS. *Journal of Atmospheric and Solar-Terrestrial Physics*, 59(6), 669–673. [https://doi.org/10.1016/S1364-6826\(96\)00102-2](https://doi.org/10.1016/S1364-6826(96)00102-2)

Emmert, J. T., Drob, D. P., Shepherd, G. G., Hernandez, G., Jarvis, M. J., Meriwether, J. W., & Tepley, C. A. (2008). DWM07 global empirical model of upper thermospheric storm-induced disturbance winds. *Journal of Geophysical Research*, 113, A11319. <https://doi.org/10.1029/2008JA013541>

Englert, C. R., Harlander, J. M., Brown, C. M., & Marr, K. D. (2015). Spatial heterodyne spectroscopy at the Naval Research Laboratory. *Applied Optics*, 54(31), F158–F163. <https://doi.org/10.1364/AO.54.00F158>

Englert, C. R., Harlander, J. M., Brown, C. M., Marr, K. D., Miller, I. J., Stump, J. E., & Immel, T. J. (2017). Michelson Interferometer for Global High-resolution Thermospheric Imaging (MIGHTI): Instrument design and calibration. *Space Science Reviews*, 212(1), 553–584. <https://doi.org/10.1007/s11214-017-0358-4>

Englert, C. R., Harlander, J., Brown, C., Meriwether, J., Makela, J., Castelaz, M., & Marr, K. (2012). Coincident thermospheric wind measurements using ground-based Doppler Asymmetric Spatial Heterodyne (DASH) and Fabry-Perot Interferometer (FPI) instruments. *Journal of Atmospheric and Solar-Terrestrial Physics*, 86, 92–98. <https://doi.org/10.1016/j.jastp.2012.07.002>

Fejer, B. G., Emmert, J. T., & Sipler, D. P. (2002). Climatology and storm time dependence of nighttime thermospheric neutral winds over Millstone Hill. *Journal of Geophysical Research*, 107(A5), SIA31–SIA39. <https://doi.org/10.1029/2001JA000300>

Forbes, J. M., Bruinsma, S. L., Doornbos, E., & Zhang, X. (2016). Gravity wave-induced variability of the middle thermosphere. *Journal of Geophysical Research: Space Physics*, 121(7), 6914–6923. <https://doi.org/10.1002/2016JA022923>

Gault, W. A., Thuillier, G., Shepherd, G. G., Zhang, S. P., Wiens, R. H., Ward, W. E., & Vincent, R. A. (1996). Validation of O(¹S) wind measurements by WINDII: the WIND Imaging Interferometer on UARS. *Journal of Geophysical Research*, 101(D6), 10405–10430. <https://doi.org/10.1029/95JD03352>

Harding, B. J., Gehrels, T. W., & Makela, J. J. (2014). Nonlinear regression method for estimating neutral wind and temperature from Fabry-Perot interferometer data. *Applied Optics*, 53(4), 666–673. <https://doi.org/10.1364/AO.53.000666>

Harding, B. J., Makela, J. J., Englert, C. R., Marr, K. D., Harlander, J. M., England, S. L., & Immel, T. J. (2017). The MIGHTI wind retrieval algorithm: Description and verification. *Space Science Reviews*, 212(1), 585–600. <https://doi.org/10.1007/s11214-017-0359-3>

Harding, B. J., Makela, J. J., Qin, J., Fisher, D. J., Martinis, C. R., Noto, J., & Wrasse, C. M. (2017). Atmospheric scattering effects on ground-based measurements of thermospheric vertical wind, horizontal wind, and temperature. *Journal of Geophysical Research: Space Physics*, 122(7), 7654–7669. <https://doi.org/10.1002/2017JA023942>

Harding, B. J., Ridley, A. J., & Makela, J. J. (2019). Thermospheric weather as observed by ground-based FPIs and modeled by GITM. *Journal of Geophysical Research: Space Physics*, 124(2), 1307–1316. <https://doi.org/10.1029/2018JA026032>

Hays, P. B., & HRDI Science Team (1992). Remote sensing of mesospheric winds with the high-resolution Doppler imager. *Planetary and Space Science*, 40(12), 1599–1606. [https://doi.org/10.1016/0032-0633\(92\)90119-9](https://doi.org/10.1016/0032-0633(92)90119-9)

Hernandez, G., & Roble, R. (1979). Thermospheric dynamics investigations with very high resolution spectrometers. *Applied Optics*, 18(20), 3376–3385. <https://doi.org/10.1364/AO.18.003376>

Immel, T. J., England, S. L., Mende, S. B., Heelis, R. A., Englert, C. R., Edelstein, J., & Sirk, M. M. (2017). The ionospheric connection explorer mission: Mission goals and design. *Space Science Reviews*, 214(1), 13. <https://doi.org/10.1007/s11214-017-0449-2>

Kaab, M., Bernalhoulden, Z., Fisher, D. J., Harding, B., Bouhir, A., Makela, J. J., & Lazrek, M. (2017). Climatology of thermospheric neutral winds over Oukaimeden Observatory in Morocco. *Annales Geophysicae*, 35(1), 161–170. <https://doi.org/10.5194/angeo-35-161-2017>

Kelley, M. C. (2009). *The Earth's ionosphere: Plasma physics & electrodynamics* (2nd ed. 96). Academic Press.

Lathuillière, C., Lilensten, J., Gault, W., & Thuillier, G. (1997). Meridional wind in the auroral thermosphere: Results from EISCAT and WINDII-O(¹D) coordinated measurements. *Journal of Geophysical Research: Space Physics*, 102(A3), 4487–4492. <https://doi.org/10.1029/96JA03429>

Link, R., & Cogger, L. L. (1988). A reexamination of the O I 6300-Å nightglow. *Journal of Geophysical Research*, 93(A9), 9883–9892. <https://doi.org/10.1029/JA093iA09p09883>

Lu, X., Liu, A. Z., Swenson, G. R., Li, T., Leblanc, T., & McDermid, I. S. (2009). Gravity wave propagation and dissipation from the stratosphere to the lower thermosphere. *Journal of Geophysical Research*, 114, D11101. <https://doi.org/10.1029/2008JD010112>

Makela, J. J., Fisher, D. J., Meriwether, J. W., Buriti, R. A., & Medeiros, A. F. (2013). Near-continual ground-based nighttime observations of thermospheric neutral winds and temperatures over equatorial Brazil from 2009 to 2012. *Journal of Atmospheric and Solar-Terrestrial Physics*, 103, 94–102. <https://doi.org/10.1016/j.jastp.2012.11.019>

Makela, J. J., Meriwether, J. W., Huang, Y., & Sherwood, P. J. (2011). Simulation and analysis of a multi-order imaging Fabry-Perot interferometer for the study of thermospheric winds and temperatures. *Applied Optics*, 50(22), 4403–4416. <https://doi.org/10.1364/AO.50.004403>

Makela, J. J., Meriwether, J. W., Lima, J. P., Miller, E. S., & Armstrong, S. J. (2009). The remote equatorial nighttime observatory of ionospheric regions project and the international heliospherical year. *Earth, Moon, and Planets*, 104(1), 211–226. <https://doi.org/10.1007/s11038-008-9289-0>

Makela, J. J., Meriwether, J. W., Ridley, A. J., Ciocca, M., & Castellez, M. W. (2012). Large-scale measurements of thermospheric dynamics with a multisite Fabry-Perot interferometer network: Overview of plans and results from midlatitude measurements. *International Journal of Geophysics*, 2012, 872140. <https://doi.org/10.1155/2012/872140>

Meriwether, J. (2006). Studies of thermospheric dynamics with a Fabry-Perot interferometer network: A review. *Journal of Atmospheric and Solar-Terrestrial Physics*, 68(13), 1576–1589.

Meriwether, J., Makela, J., Fisher, D., Buriti, R., Medeiros, A., Akmaev, R., & Wu, F. (2013). Comparisons of thermospheric wind and temperature measurements in equatorial Brazil to whole atmosphere model predictions. *Journal of Atmospheric and Solar-Terrestrial Physics*, 103, 103–112. <https://doi.org/10.1016/j.jastp.2013.04.002>

Navarro, L. A., & Fejer, B. G. (2019). Storm-time thermospheric winds over Peru. *Journal of Geophysical Research: Space Physics*, 124(12), 10415–10427. <https://doi.org/10.1029/2019JA027256>

Navarro, L. A., & Fejer, B. G. (2020). Storm-time coupling of equatorial nighttime F region neutral winds and plasma drifts. *Journal of Geophysical Research: Space Physics*, 125(9), e2020JA028253. <https://doi.org/10.1029/2020JA028253>

Richmond, A. D. (1978). Gravity wave generation, propagation, and dissipation in the thermosphere. *Journal of Geophysical Research*, 83(A9), 4131–4145. <https://doi.org/10.1029/JA083iA09p04131>

Richmond, A. D. (1979). Thermospheric heating in a magnetic storm: Dynamic transport of energy from high to low latitudes. *Journal of Geophysical Research*, 84(A9), 5259–5266. <https://doi.org/10.1029/JA084iA09p05259>

Richmond, A. D., & Matsushita, S. (1975). Thermospheric response to a magnetic substorm. *Journal of Geophysical Research*, 80(19), 2839–2850. <https://doi.org/10.1029/JA080i019p02839>

Rishbeth, H. (1972). Superrotation of the upper atmosphere. *Reviews of Geophysics*, 10(3), 799–819. <https://doi.org/10.1029/RG010i003p00799>

Rishbeth, H., & Garriot, O. (1969). *Introduction to ionospheric physics* (1st ed.). New York, NY: Academic Press.

Shepherd, G. G., Thuillier, G., Cho, Y.-M., Duboin, M.-L., Evans, W. F. J., Gault, W. A., & Ward, W. E. (2012). The Wind Imaging Interferometer (WINDII) on the Upper Atmosphere Research Satellite: A 20 year perspective. *Reviews of Geophysics*, 50(2). <https://doi.org/10.1029/2012RG000390>

Shepherd, G. G., Thuillier, G., Gault, W. A., Solheim, B. H., Hersom, C., Alunni, J. M., & Wimperis, J. (1993). WINDII, the wind imaging interferometer on the Upper Atmosphere Research Satellite. *Journal of Geophysical Research*, 98(D6), 10725–10750. <https://doi.org/10.1029/93JD00227>

Shiokawa, K., Otsuka, Y., Ogawa, T., Kawamura, S., Yamamoto, M., Fukao, S., & Yumoto, K. (2003). Thermospheric wind during a storm-time large-scale traveling ionospheric disturbance. *Journal of Geophysical Research*, 108, 1423. <https://doi.org/10.1029/2003JA010001>

Vadas, S. L. (2007). Horizontal and vertical propagation and dissipation of gravity waves in the thermosphere from lower atmospheric and thermospheric sources. *Journal of Geophysical Research*, 112, A06305. <https://doi.org/10.1029/2006JA011845>

Vadas, S. L., & Fritts, D. C. (2004). Thermospheric responses to gravity waves arising from mesoscale convective complexes. *Journal of Atmospheric and Solar-Terrestrial Physics*, 66(6), 781–804. <https://doi.org/10.1016/j.jastp.2004.01.025>

Wu, Y.-J. J., Harding, B. J., Triplett, C. C., Makela, J. J., Marr, K. D., Englert, C. R., & Immel, T. J. (2020). Errors from asymmetric emission rate in spaceborne, limb sounding Doppler interferometry: A correction algorithm with application to icon/mighti. *Earth and Space Science*, 7(10), e2020EA001164. <https://doi.org/10.1029/2020EA001164>

Xiong, C., Lühr, H., & Fejer, B. G. (2015). Global features of the disturbance winds during storm time deduced from CHAMP observations. *Journal of Geophysical Research: Space Physics*, 120(6), 5137–5150. <https://doi.org/10.1002/2015JA021302>

Xiong, C., Lühr, H., & Yamazaki, Y. (2019). An opposite response of the low-latitude ionosphere at Asian and American sectors during storm recovery phases: drivers from below or above. *Journal of Geophysical Research: Space Physics*, 124(7), 6266–6280. <https://doi.org/10.1029/2019JA026917>